available at www.sciencedirect.com
journal homepage: www.europeanurology.com

European Association of Urology

Platinum Priority – Brief Correspondence

Editorial by Jonathan E. Shoag, Jeffrey J. Tosoian, Simpa S. Salami and Christopher E. Barbieri on pp. 24–26 of this issue

Molecular Hallmarks of Multiparametric Magnetic Resonance Imaging Visibility in Prostate Cancer

Kathleen E. Houlahan [a,b,c,†], Amirali Salmasi [d,†], Taylor Y. Sadun [d], Aydin Pooli [d], Ely R. Felker [e], Julie Livingstone [a], Vincent Huang [a], Steven S. Raman [e], Preeti Ahuja [e], Anthony E. Sisk Jr. [f], Paul C. Boutros [a,b,c,d,g,h,i,j,l,], Robert E. Reiter [d,i,k,m,*]*

[a] *Ontario Institute for Cancer Research, Toronto, Canada;* [b] *Department of Medical Biophysics, University of Toronto, Toronto, Canada;* [c] *Vector Institute, Toronto, Canada;* [d] *Department of Urology, David Geffen School of Medicine, University of California, Los Angeles, CA, USA;* [e] *Department of Radiology, David Geffen School of Medicine, University of California, Los Angeles, CA, USA;* [f] *Department of Pathology, David Geffen School of Medicine, University of California, Los Angeles, CA, USA;* [g] *Department of Pharmacology and Toxicology, University of Toronto, Toronto, Canada;* [h] *Department of Human Genetics, University of California, Los Angeles, CA, USA;* [i] *Jonsson Comprehensive Cancer Center, David Geffen School of Medicine, University of California, Los Angeles, CA, USA;* [j] *Institute for Precision Health, University of California, Los Angeles, CA, USA;* [k] *Institute of Urologic Oncology, University of California, Los Angeles, CA, USA;* [l] *UCLA Department of Human Genetics, 10833 Le Conte Avenue, Los Angeles, CA 90095;* [m] *Department of Urology, David Geffen School of Medicine, 300 Stein Plaza, Los Angeles, CA 90095, USA*

Article info

Article history:
Accepted December 20, 2018

Associate Editor:
James Catto

Keywords:
Prostate cancer
Multiparametric magnetic resonance imaging visibility
Radiogenomics
Nimbosus
Transcriptomics

Abstract

Multiparametric magnetic resonance imaging (mpMRI) has transformed the management of localized prostate cancer by improving identification of clinically significant disease at diagnosis. Approximately 20% of primary prostate tumors are invisible to mpMRI, and we hypothesize that this invisibility reflects fundamental molecular properties of the tumor. We therefore profiled the genomes and transcriptomes of 40 International Society of Urological Pathology grade 2 tumors: 20 mpMRI-invisible (Prostate Imaging-Reporting and Data System [PI-RADS] v2 <3) and 20 mpMRI-visible (PI-RADS v2 5) tumors. mpMRI-visible tumors were enriched in hallmarks of nimbosus, an aggressive pathological, molecular, and microenvironmental phenomenon in prostate cancer. These hallmarks included genomes with increased mutation density, a higher prevalence of intraductal carcinoma/cribriform architecture pathology, and altered abundance of 102 transcripts, including overexpression of noncoding RNAs such as *SCHLAP1*. Multiple small nucleolar RNAs (snoRNAs) were identified, and a snoRNA signature synergized with nimbosus hallmarks to discriminate visible from invisible tumors. These data suggest a confluence of aggressive molecular and microenvironmental phenomena underlie mpMRI visibility of localized prostate cancer.

Patient summary: We examined the correlation between tumor biology and magnetic resonance imaging (MRI) visibility in a group of patients with low- intermediate-risk prostate cancer. We observed that MRI findings are associated with biological features of aggressive prostate cancer.

† These authors contributed equally to this work.
* Corresponding authors.
E-mail addresses: Paul.Boutros@oicr.on.ca (P.C. Boutros), RReiter@mednet.ucla.edu (R.E. Reiter).

https://doi.org/10.1016/j.eururo.2018.12.036
0302-2838/

Improved clinical risk stratification remains a pressing concern for localized prostate cancer, with current treatment guidelines leading to both over- and undertreatment for many patients. One promising solution to this challenge is diffusion-weighted multiparametric magnetic resonance imaging (mpMRI) with dynamic contrast enhancement. Prostate Imaging-Reporting and Data System version 2 (PI-RADS v2) provides international standardized guidelines for scoring images on a five-point scale that reflects the likelihood of clinically significant disease, with PI-RADS v2 scores of 1 and 5 representing a very low and a very high likelihood of disease, respectively [1]. PI-RADS v2 scores accurately predict clinically significant disease [2,3]. Although many tumors are invisible to mpMRI, insight into the molecular hallmarks of mpMRI visibility is sparse. The presence of mpMRI-visible International Society of Urological Pathology (ISUP) grade 1 tumors and mpMRI-invisible ISUP grade 5 tumors suggests functional differences between otherwise histologically similar tumors. We therefore hypothesized that mpMRI visibility of individual tumors is driven by specific genomic features, with high PI-RADS v2 tumors preferentially harboring molecular hallmarks of aggressiveness [4].

We profiled the transcriptomic and copy number profile of 40 clinically significant invisible and visible tumors, all with ISUP grade 2 disease and treated by radical prostatectomy. Each case underwent presurgical mpMRI and final pathology revealed a solitary ISUP grade 2 lesion larger than 1.5 cm. Twenty tumors were mpMRI-invisible (PI-RADS v2 score <3) and 20 tumors were mpMRI-visible (PI-RADS v2 score 5; Fig. 1A; Supplementary Table 1). To avoid confounding by zonal origin, tumors of the peripheral zone (PZ) and transition zone (TZ) were equally represented in both groups (12 PZ and 8 TZ per group; Table 1; Supplementary Table 1). Prostate and tumor volume were weakly correlated in the invisible ($\rho = 0.35$) and visible groups ($\rho = 0.54$; Supplementary Fig. 1). Clinical characteristics alone could not predict tumor visibility (area under the receiver operating characteristic curve [AUC] 0.60, 95% confidence interval [CI] 0.41–0.80; Supplementary Fig. 1). The groups did not differ in tumor cellularity (Mann-Whitney test, $p = 0.5$; Supplementary Table 1). As expected, the percentage of grade 4 architecture was greater for mpMRI-visible than for mpMRI-invisible tumors (Mann-Whitney test, $p < 0.001$; Table 1; Supplementary Table 1). This is consistent with literature demonstrating that MRI visibility correlates with, but does not explain, Gleason score [5,6]. Retrospective blinded review identified five patients with PI-RADS v2 3 lesions and one with a PI-RADS v2 4 lesion (Supplementary Table 1), consistent with reported interobserver variability of $\kappa = 0.42–0.63$ for PI-RADS v2 [7,8].Importantly, no mpMRI-invisible tumors were regraded as PI-RADS v2 5.

To identify molecular hallmarks of mpMRI visibility, copy number aberrations (CNAs) and mRNA abundance were profiled for each tumor; these recapitulated known subtypes (Supplementary Fig. 2). RNA and CNA profiling was highly concordant, with 69% of recurrently deleted genes showing lower mRNA abundance (Supplementary Fig. 3). Our sample size provided power to detect differential abundance between the visibility states for 11,604 genes (power >0.80 at $|\log_2$ fold change [FC]$| \geq 1$; Supplementary Fig. 3). Univariate analysis identified 102 transcripts differentially abundant between visible and invisible tumors, with 61% more abundant in visible tumors (false discovery rate [FDR] <0.05; Fig. 1B; Supplementary Table 2). Next, we investigated pathway enrichment in these differentially abundant transcripts and determined that the transcripts were not enriched in any one particular pathway. This suggests that mpMRI visibility may be a result of dysregulation of multiple rather than a single pathway; the differentially abundant transcripts included many genes involved in prostate cancer progression. For example, *ANKRD30A* (NY-BR-1) was ~200-fold more abundant in visible tumors ($\log_2$ FC = 7.6; FDR < 0.001; Fig. 1C), and is a tumor-specific antigen present in ~30% of prostate tumors that selectively activates $CD8^+$ T cells [9]. Similarly, the peptide hormone relaxin 1 was approximately fourfold more abundant in visible tumors ($\log_2$ FC = 2.4; FDR = 0.02; Fig. 1D); it promotes prostate cancer progression via increases in cell motility and androgen receptor activity [10]. Conversely, the histone methyltransferase *KMT2D* ($\log_2$ FC = −0.60; FDR = 0.04) and the hypoxia inducible factor *EGLN2* ($\log_2$ FC = −0.86, FDR = 0.02) were significantly more abundant in invisible tumors (Supplementary Fig. 3).

Unexpectedly, noncoding transcripts comprised the majority of differentially abundant RNAs (57/102). In particular, small nucleolar RNAs (snoRNAs) were significantly more likely to have elevated abundance in visible tumors (odds ratio [OR] 4.4; FDR = 0.002; Fisher's exact test; Fig. 1E). Altered snoRNAs were drawn from multiple families, including three C/D box (*SNORD33*, *SNORD3A*, and *SNORD68*), three H/ACA box (*SNORA12*, *SNORA37*, and *SNORA54*), and one small Cajal body-specific RNA (*SCARNA5*; Supplementary Fig. 4). snoRNA enrichment was independent of host gene abundance (Supplementary Fig. 4). We created a snoRNA signature that accurately discriminated invisible tumors (AUC 0.76, 95% CI 0.60–0.92; Fig. 1F). This snoRNA signature follows a pan-cancer report that snoRNAs are significantly more abundant in tumor than in matched normal tissue [11]. Moreover, independent efforts have highlighted the role of snoRNAs in tumorigensis, specifically snoRNA U50 [12,13] and snoRNA 93 [14]. Indeed, two of the seven snoRNAs identified (SNORA37 and SNORA12) were prognostic: high abundance was associated with rapid biochemical recurrence in an independent intermediate-risk prostate cancer cohort (hazard ratio 2.00 and 2.00; $p = 0.053$ and 0.051; EGAS00001000900; Supplementary Fig. 4). Finally, several other key noncoding transcripts were associated with mpMRI visibility. In particular, *TERC*, which encodes the telomerase RNA component and contains a H/ACA snoRNA-like domain at its 3′ end [15], was more abundant in visible tumors ($\log_2$ FC = 1.6; FDR = 0.04; Supplementary Fig. 4).

Perhaps most provocatively, *SCHLAP1*, a long noncoding RNA linked to prostate cancer progression [16], was more abundant in visible tumors ($\log_2$ FC = 3.2, FDR = 0.03; Fig. 2A)

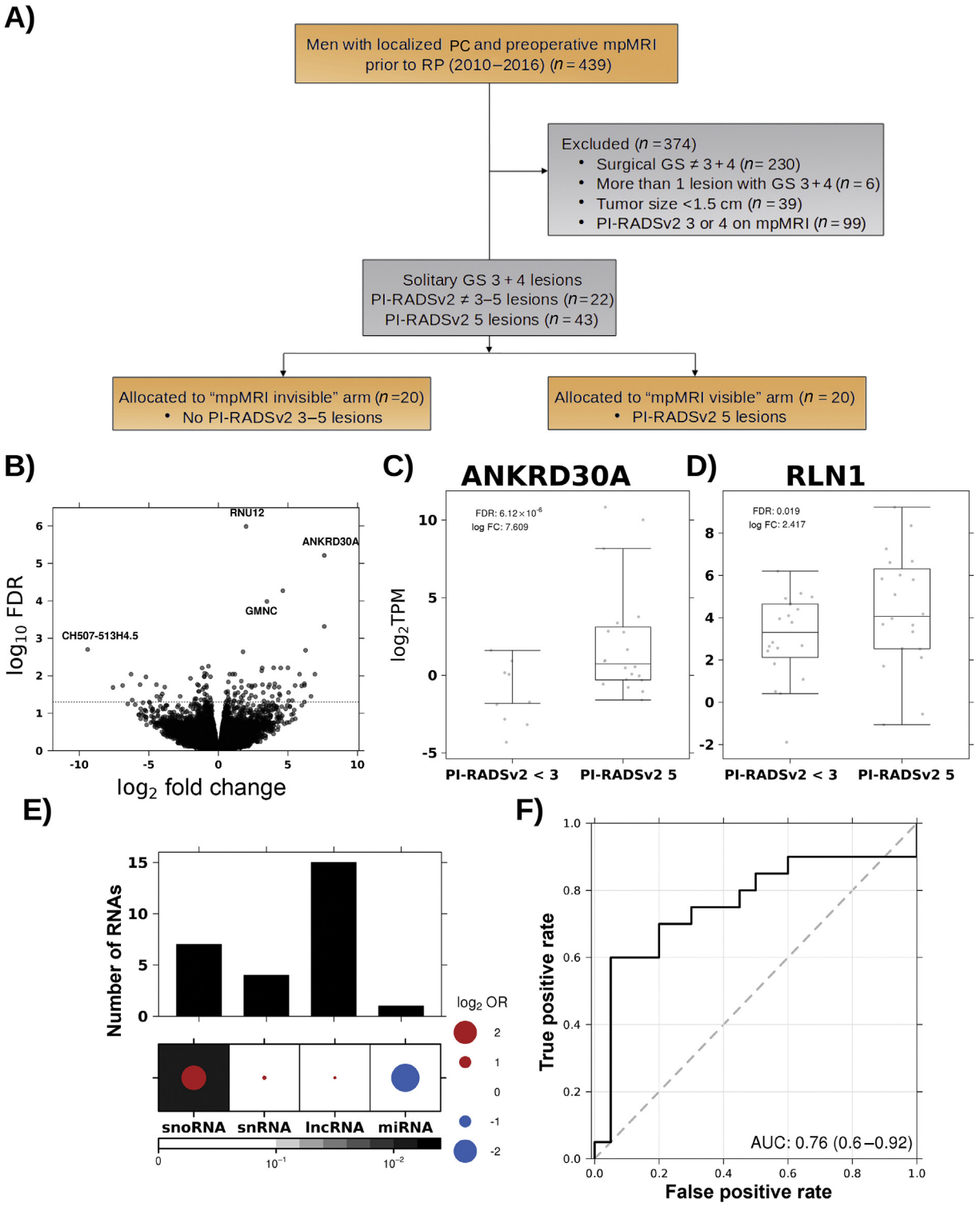

Fig. 1 – Transcriptomic basis of mpMRI visibility. (A) Outline of the study design, highlighting the criteria for patient inclusion and exclusion. (B) Differentially abundant RNAs in PI-RADS v2 5 versus <3 tumors as determined using a negative binomial generalized log-linear model. The horizontal dotted line indicates a false discovery rate (FDR) of 0.05. (C) *ANKRD30A* and (D) *RLN1* are upregulated in PI-RADS v2 5 tumors. The FC and FDR are from a negative binomial generalized log-linear model and box plots show the 25% quartile, median, and 75% quartile. (E) The subset of differentially abundant RNAs were enriched in snoRNAs. The top plot indicates the number of each noncoding RNA in the subset and the dot map indicates the enrichment of each RNA. The size of the circle reflects the OR in $\log_2$ space for easier visualization while the circle color denotes if the raw OR is >1 (red) or <1 (blue). The background shading indicates the FDR (Fisher's exact test). (F) A snoRNA signature accurately predicted PI-RADS v2 5 tumors with 76% accuracy. PC = prostate cancer; mpMRI = multiparametric magnetic resonance imaging; RP = radical prostatectomy; GS = Gleason score; PI-RADS = Prostate Imaging-Reporting and Data System; snoRNA = small nucleolar RNA; lncRNA = long noncoding RNA; miRNA = microRNA; FC = fold change; FDR = false discovery rate; TPM = transcripts per kilobase million; OR = odds ratio; AUC = area under the receiver operating characteristic curve.

Table 1 – Summary of characteristics for patients selected for the mpMRI-invisible and -visible groups

Variables	Invisible lesions (PI-RADS v2 ≠ 3–5)	Visible lesions (PI-RADS v2 5)	*p* value[a]
Patients (*n*)	20	20	–
Median age, yr (IQR)	60.5 (54–67)	64 (56–71)	0.38
Median PSA, ng/ml (IQR)	6.5 (4.5–7.4)	6.6 (5.0–9.7)	0.35
Median PSA density, ng/ml^2 (IQR)	0.15 (0.10–0.2)	0.16 (0.10–0.26)	0.47
Median pathologic prostate volume, ml (IQR)	41 (34–53)	45 (32–52)	0.98
Median tumor size, cm (IQR)	2.1 (1.8–2.7)	2.8 (2.0–3.3)	0.12
Median tumor volume, ml (IQR)	4.3 (2.4–7.8)	6.5 (4.5–10.1)	0.03*
Pathologic staging, *n* (%)			0.05
T2	16 (80)	9 (45)	
T3	4 (20)	11 (55)	
Tumor location, *n* (%)			1.00
Peripheral zone	12 (60)	12 (60)	
Transitional zone	8 (40)	8 (40)	
Gleason 4 pattern, *n* (%)			1.0×10^{-5}*
<5%	5 (25)	0 (0)	
5–10%	12 (60)	5 (25)	
11–30%	3 (15)	8 (40)	
>30%	0 (0)	7 (35)	
Cribriform architecture, *n* (%)			0.09
<5%	18 (90)	11 (55)	
5–10%	2 (10)	7 (35)	
11–30%	0	2 (10)	
Intraductal carcinoma, *n* (%)			0.42
<5%	20 (100)	18 (90)	
5–10%	0	1 (5)	
11–30%	0	1 (5)	

mpMRI = multiparametric magnetic resonance imaging; PI-RADS = Prostate Imaging-Reporting and Data System; IQR = interquartile range; PSA = prostate-specific antigen.

* Significant difference between the groups.

[a] Mann-Whitney test except for pathologic staging and tumor location (Fisher's exact test).

and the higher abundance could not be explained by CNAs ($\log_2$ FC = −0.39; $p = 0.7$; Supplementary Fig. 4). *SCHLAP1* abundance fell within the expected range for ISUP grade 2 prostate tumors (EGAS00001000900; Supplementary Fig. 4), but on its own could not accurately predict mpMRI visibility (AUC 0.60, 95% CI 0.41–0.80; Supplementary Fig. 4). Therefore, we next considered nimbosus, a phenomenon characterized by the co-occurrence of pathological, molecular, and microenvironmental events, including intraductal carcinoma and cribriform architecture (IDC/CA), genomic instability, *SCHLAP1* expression, and hypoxia [17]. This co-occurrence results in an aggressive tumor phenotype with poor patient outcomes. *SCHLAP1* enrichment in visible tumors suggested that nimbosus might be associated with mpMRI visibility, which prompted us to investigate its other hallmarks. We quantified genomic instability as the percentage of the genome altered via CNAs (PGA). PGA was elevated in visible tumors ($p = 0.03$; $\beta = 0.6$ adjusted for tumor purity; Fig. 2B), driven by longer average length of individual amplifications and deletions (Supplementary Fig. 5). Concordantly, IDC/CA was more frequent in visible tumors (OR 7.0; $p = 0.03$; Fig. 2C). CA and IDC subsets were of particular interest as their visibility on mpMRI has been debated [18,19], and are associated with advanced disease [18,20] and worse disease specific survival [21,22]. Interestingly, there was no difference in hypoxia levels between the groups, regardless of gene signature used to quantify hypoxia (Fig 2D; Supplementary Fig 5). Both PGA and hypoxia measurements fell within the expected range for ISUP grade 2 prostate cancer tumors (Supplementary Fig. 5) [23]. These hallmarks were not driven by the five tumors with upgraded PI-RADS v2 scores on blinded retrospective review or by the percentage Gleason 4 in the tumor (Supplementary Fig. 5). Indeed, *SCHLAP1* mRNA abundance was still significantly greater in PI-RADS v2 5 tumors after removing the upgraded invisible tumors ($\log_2$ FC = 2.75; $p = 0.03$, Mann-Whitney test), and *SCHLAP1* mRNA and PGA were only weakly correlated with percentage Gleason 4 in visible tumors (Spearman correlation $\rho = 0.33$ and 0.19; $p = 0.15$ and 0.4; Supplementary Fig. 5). Finally, because hallmarks were not strongly correlated (Supplementary Fig. 6), we looked at synergy between them and found that the odds of visibility were tenfold higher with co-occurrence of two or more hallmarks (OR 10; $p = 5.7 \times 10^{-3}$; Fig. 2E). These are exploratory analyses requiring further validation. Nevertheless, nimbosus hallmarks synergized with snoRNA levels to predict visibility with 87% accuracy, superior to the 60% accuracy of a clinical signature (Supplementary Fig. 1), suggesting that elevated snoRNA abundance may be a novel hallmark of nimbotic tumors (AUC 0.87, 95% CI 0.75–0.99; Fig. 2F). This represents a promising preliminary signature of mpMRI visibility for future validation studies.

This work points to a novel model for the origin of mpMRI visibility involving the co-occurrence of multiple aggressive hallmarks reminiscent of nimbosus. These hallmarks include IDC/CA pathology, increased PGA and overexpression of key non-coding transcripts, such as *SCHLAP1* and snoRNAs. We note that our cohort size was limited to detecting large

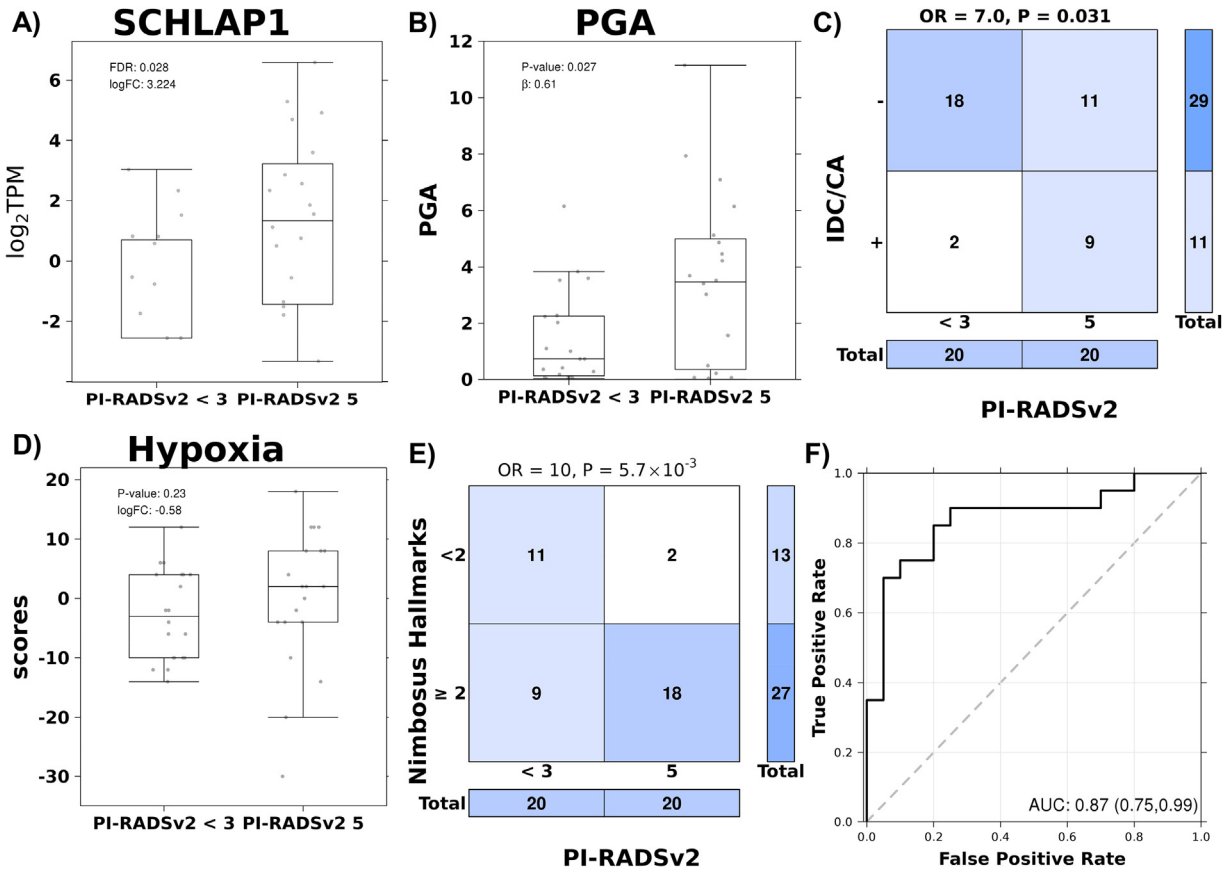

Fig. 2 – Nimbosus drives mpMRI visibility. (A) *SCHLAP1* was upregulated in PI-RADS v2 5 tumors as determined from a negative binomial generalized log-linear model. The box plot shows the 25% quartile, median, and 75% quartile. (B) PGA was upregulated in PI-RADS v2 5 tumors; the *p* value is from logistic regression after adjusting for tumor purity. (C) PI-RADS v2 5 tumors were enriched in IDC/CA. OR and *p* value from Fisher's exact test. (D) Hypoxia, quantified using the Ragnum signature (Supplementary material), was not significantly different between conditions (*p* value from Mann-Whitney test). (E) The co-occurrence of two or more nimbosus hallmarks increased the odds of a PI-RADS v2 5 tumor. OR and *p* value from Fisher's exact test. (F) Nimbosus hallmarks synergize with the small nucleolar RNA signature to accurately predict PI-RADS v2 5 tumors with 87% accuracy. mpMRI = multiparametric magnetic resonance imaging; PI-RADS = Prostate Imaging-Reporting and Data System; TPM = transcripts per kilobase million; FC = fold change; FDR = false discovery rate; PGA = percentage of the genome changed via copy number alterations; IDC/CA = intraductal carcinoma/cribriform architecture; OR = odds ratio; AUC = area under the receiver operating characteristic curve.

transcriptomic alterations ($\log_2$ FC $\geq$ 0.6; Supplementary Fig. 3) and that our single-region sampling does not fully represent the spatial heterogeneity of the tumor. The tumor areas of interest were selected with the guidance of a uropathologist to reflect architecture representative of the tumor as a whole, and the relevant areas of tissue were macrodissected for nucleic acid extraction. An entire tumor may not be visible (even for tumors with PI-RADS v2 5 lesions), and invisible portions of PI-RADS v2 5 tumors included in this analysis will lead to underestimation of molecular differences. Thus, this work serves as a lower bound for the differences between visible and invisible tumors. Similarly, our study has higher power for events earlier in evolution—those common to invisible and visible regions of tumor—which again underestimates true molecular differences. Finally, it is important to note that characterization of the hypoxic microenvironment was conducted on surgically resected tissue. Molecular signatures of hypoxia do not account for variable operative time that could lead to nonuniform molecular degradation. In vivo quantification techniques, such as ultrasound-guided transrectal needle Eppendorf electrodes [24], are required for more accurate characterization of a hypoxic microenvironment. This work highlights the clinical utility of integrated radiogenomic models for stratifying indolent versus aggressive disease and presents a novel model for mpMRI visibility. Our data suggest a confluence of aggressive transcriptomic, genomic, and pathological hallmarks required for mpMRI visibility, providing a molecular basis for the observation that visible tumors are clinically more aggressive.

Author contributions: Paul C. Boutros had full access to all the data in the study and takes responsibility for the integrity of the data and the accuracy of the data analysis.

Study concept and design: Reiter, Boutros.
Acquisition of data: Pooli, Salmasi, Felker, Raman, Ahuja.
Analysis and interpretation of data: Houlahan, Livingstone, Huang, Boutros, Reiter.
Drafting of the manuscript: Houlahan, Salmasi, Sadun, Reiter, Boutros.
Critical revision of the manuscript for important intellectual content: Houlahan, Salmasi, Sadun, Pooli, Felker, Livingstone, Huang, Raman, Ahuja, Sisk, Boutros, Reiter.

Statistical analysis: Houlahan.
Obtaining funding: Boutros, Reiter.
Administrative, technical, or material support: None.
Supervision: Boutros, Reiter.
Other (pathology analysis): Sisk.

Financial disclosures: Paul C. Boutros certifies that all conflicts of interest, including specific financial interests and relationships and affiliations relevant to the subject matter or materials discussed in the manuscript (eg, employment/affiliation, grants or funding, consultancies, honoraria, stock ownership or options, expert testimony, royalties, or patents filed, received, or pending), are the following: None.

***Funding/Support and role of the sponsor*:** This study was conducted with the support of the UCLA SPORE In Prostate Cancer, NIH/NCI grant number P50 CA092131. The sponsor played a role in data collection.

Acknowledgments: The authors thank all members of the Boutros laboratory for helpful suggestions and support. Paul C. Boutros was supported by a Terry Fox Research Institute New Investigator Award, a CIHR New Investigator Award, a CIHR project grant, the Canadian Cancer Society (grant #705649), and a CIHR CEEHRC grant. Kathleen E. Houlahan was supported by a CIHR Vanier fellowship. Taylor Y. Sadun was supported by a H&H Lee Surgical Research Grant and a Jerry Janger fellowship.

Appendix A. Supplementary data

Supplementary data associated with this article can be found, in the online version, at https://doi.org/10.1016/j.eururo.2018.12.036.

References

[1] Weinreb JC, Barentsz JO, Choyke PL, et al. PI-RADS Prostate Imaging-Reporting and Data System: 2015, version 2. Eur Urol 2016;69:16–40.
[2] Almeida GL, Petralia G, Ferro M, et al. Role of multi-parametric magnetic resonance image and PIRADS score in patients with prostate cancer eligible for active surveillance according PRIAS criteria. Urol Int 2016;96:459–69.
[3] Kasivisvanathan V, Rannikko AS, Borghi M, et al. MRI-targeted or standard biopsy for prostate-cancer diagnosis. N Engl J Med 2018;378:1767–77.
[4] Lalonde E, Ishkanian AS, Sykes J, et al. Tumor genomic and microenvironmental heterogeneity for integrated prediction of 5-year biochemical recurrence of prostate cancer: a retrospective cohort study. Lancet Oncol 2014;15:1521–32.
[5] Le JD, Tan N, Shkolyar E, et al. Multifocality and prostate cancer detection by multiparametric magnetic resonance imaging: correlation with whole-mount histopathology. Eur Urol 2015;67:569–76.
[6] Filson CP, Natarajan S, Margolis DJ, et al. Prostate cancer detection with magnetic resonance-ultrasound fusion biopsy: the role of systematic and targeted biopsies. Cancer 2016;122:884–92.
[7] Muller BG, Shih JH, Sankineni S, et al. Prostate cancer: interobserver agreement and accuracy with the revised Prostate Imaging Reporting and Data System at multiparametric MR imaging. Radiology 2015;277:741–50.
[8] Purysko AS, Bittencourt LK, Bullen JA, et al. Accuracy and interobserver agreement for Prostate Imaging Reporting and Data System, version 2, for the characterization of lesions identified on multiparametric MRI of the prostate. Am J Roentgenol 2017;209:339–49.
[9] Jäger D, Karbach J, Pauligk C, et al. Humoral and cellular immune responses against the breast cancer antigen NY-BR-1: definition of two HLA-A2 restricted peptide epitopes. Cancer Immun 2005;5:11.
[10] Thompson VC, Hurtado-Coll A, Turbin D, et al. Relaxin drives Wnt signaling through upregulation of PCDHY in prostate cancer. Prostate 2010;70:1134–45.
[11] Gong J, Li Y, Liu CH, et al. A pan-cancer analysis of the expression and clinical relevance of small nucleolar RNAs in human cancer. Cell Rep 2017;21:1968–81.
[12] Dong XY, Rodriguex C, Guo P, et al. SnoRNA U50 is a candidate tumor-suppressor gene at 6q14.3 with a mutation associated with clinically significant prostate cancer. Hum Mol Genet 2008;17:1031–42.
[13] Dong XY, Guo P, Boyd J, et al. Implication of snoRNA U50 in human breast cancer. J Genet Genomics 2009;36:447–54.
[14] Patterson DG, Roberts JT, King VM, et al. Human snoRNA-93 is processed into a microRNA-like RNA that promotes breast cancer cell invasion. NPJ Breast Cancer 2017;3:25.
[15] Mitchell JR, Cheng J, Collins K. A box H/ACA small nucleolar RNA-like domain at the human telomerase RNA 3′ end. Mol Cell Biol 1999;19:567–76.
[16] Prensner JR, Iyer MK, Sahu A, et al. The long noncoding RNA SChLAP1 promotes aggressive prostate cancer and antagonizes the SWI/SNF complex. Nat Genet 2013;45:1392–8.
[17] Chua MLK, Lo W, Pintilie M, et al. A prostate cancer "nimbosus": genomic instability and SChLAP1 dysregulation underpin aggression of intraductal and cribriform subpathologies. Eur Urol 2017;72:665–74.
[18] Masoomian M, Downes MR, Sweet J, et al. Concordance of biopsy and prostatectomy diagnosis of intraductal and cribriform carcinoma in a prospectively collected data set. *Histopathology* 2018.
[19] Truong M, Hollenberg G, Weinberg E, et al. Impact of Gleason subtype on prostate cancer detection using multiparametric magnetic resonance imaging: correlation with final histopathology. J Urol 2017;198:316–21.
[20] Kweldam CF, Wildhagen MF, Steyerberg EW, et al. Cribriform growth is highly predictive for postoperative metastasis and disease-specific death in Gleason score 7 prostate cancer. Mod Pathol 2015;28:457–64.
[21] Kweldam CF, Kummerlin IP, Nieboer D, et al. Disease-specific survival of patients with invasive cribriform and intraductal prostate cancer at diagnostic biopsy. Mod Pathol 2016;29:630–6.
[22] Trudel D, Downes MR, Sykes J, et al. Prognostic impact of intraductal carcinoma and large cribriform carcinoma architecture after prostatectomy in a contemporary cohort. Eur J Cancer 2014;50:1610–6.
[23] Espiritu SMG, Liu LY, Rubanova Y, et al. The evolutionary landscape of localized prostate cancers drives clinical aggression. Cell 2018;173:1003–13.
[24] Parker C, Milosevic M, Toi A, et al. Polarographic electrode study of tumor oxygenation in clinically localized prostate cancer. Int J Radiat Oncol Biol Phys 2004;58:750–7.